

RESEARCH ARTICLE

Rice Phenology Mapping Using Novel Target Characterization Parameters from Polarimetric SAR Data

Subhadip Dey^a, Narayanarao Bhogapurapu^a, Avik Bhattacharya^a,
Dipankar Mandal^a, Juan M. Lopez-Sanchez^b, Heather McNairn^c and
Alejandro C. Frery^d

^aMicrowave Remote Sensing Lab, Centre of Studies in Resources Engineering, Indian
Institute of Technology Bombay, Mumbai, India;

^bInstitute for Computer Research, University of Alicante, Alicante, Spain;

^cOttawa Research and Development Centre, Agriculture and Agri-Food Canada, Ottawa,
Canada;

^dSchool of Mathematics and Statistics, Victoria University of Wellington, New Zealand

ARTICLE HISTORY

Compiled April 22, 2021

ABSTRACT

We require Spatio-temporal information about rice for executing and planning diverse management practices. In this regard, data obtained from Synthetic Aperture Radar (SAR) sensors are well suited for tracking morphological developments of rice across its phenology stages. This study proposes different target characterization parameters from polarimetric SAR data for rice phenology mapping. Six C-band Radarsat-2 images acquired over Vijayawada, India, are used for complete analysis. It is known that polarimetric information provides excellent sensitivity for identifying crop phenology stages. Hence, in this study, we assessed phenology classification results using a scattering-type parameter and scattering powers for full-polarimetric (FP) and extracted dual-polarimetric (DP) SAR data. Here, we utilized the real 4×4 Kennenough matrix elements to derive these parameters equivalently for the two polarimetric modes (i.e., FP and DP). We obtained better overall classification accuracy for each phenology stages using the proposed parameters than the existing ones from FP and DP SAR data. We noted that the overall classification accuracy using the DP SAR data was only marginally lower than the FP SAR data. This marginal difference in the accuracies could be due to the absence of the cross-polarized component in the DP SAR data. We also demonstrate the usefulness of the scattering powers from DP SAR data for rice phenology monitoring.

KEYWORDS

Supervised classification; Dual Co-pol; Radarsat-2; Phenology mapping; Full polarimetry; Model-free decomposition; Information content

CONTACT Subhadip Dey. Email: sdey2307@gmail.com Microwave Remote Sensing Lab, Centre of Studies in Resources Engineering, Indian Institute of Technology Bombay, Mumbai, India

1. Introduction

Rice is an important global crop and is a staple food grown in the Indian subcontinent. Having the requirement of large volumes of water, rice cultivation practice is generally concentrated in moderate to high rainfed areas. Throughout its cultivation period, it is essential to monitor several critical phenological stages to maximize rice productivity. These critical phenological stages include tillering, flowering and grain filling periods (Lampayan et al. 2015; Mahajan, Bharaj, and Timsina 2009). Hence, it is vital to monitor the dynamics of rice growth during these phenological stages over large production regions.

Synthetic Aperture Radar (SAR) data provide valuable information to characterize the development of rice canopies at different phenological stages. Previous studies have obtained good results for rice monitoring and mapping using X-band (Corcione et al. 2016; Yuzugullu, Erten, and Hajnsek 2015; Küçük, Taşkın, and Erten 2016; De Bernardis et al. 2015; Erten et al. 2016; Koppe et al. 2013), and C-band sensors (Zhang et al. 2014; Bouvet, Le Toan, and Lam-Dao 2009; Lopez-Sanchez et al. 2014; Yang et al. 2017; Tian et al. 2018). The radar backscattering coefficient has proven to be a good indicator of rice phenological changes. Le Toan et al. (1989) utilized dual-polarized C-band airborne SAR data to investigate the temporal backscatter response (σ_{HH}^0 and σ_{VV}^0) from rice fields. Temporal variations of σ_{HH}^0 and σ_{VV}^0 assisted in mapping rice fields according to the time of sowing and phenological stages. Similarly, radar backscatter changes over time are indicative of the phenological development of rice (Kurosu, Fujita, and Chiba 1995).

Several other studies confirmed that the temporal response of co-polarized (i.e., HH and VV) backscatter coefficients aptly capture the phenological evolution of rice (Le Toan et al. 1997; Koay et al. 2007; Bouvet, Le Toan, and Lam-Dao 2009).

62 More recently, Torbick et al. (2017) utilized the VV and VH backscatter coefficients
63 of Sentinel-1 C-band SAR data to map the spatial variation of phenological stages for
64 rice producing regions of Myanmar. Backscatter values for a given polarization are
65 useful for inferring structural information of a target, but offer limited understanding
66 of the diverse scattering mechanisms. Such features describe the complex interactions
67 of the electromagnetic (EM) wave between the soil and crop and within the canopy
68 itself. In this respect, often, scattering mechanisms are often distinguished by different
69 scattering power decomposition techniques.

70 Freeman and Durden (1998) paved the way for model-based decomposition tech-
71 niques by introducing a three-component scattering power decomposition. Later Ya-
72 maguchi et al. (2011) proposed the four-component approach incorporating the helix
73 scattering model as a fourth component. Furthermore, Cloude and Pottier (1997)
74 and Touzi (2006) decomposed the average covariance or coherency matrices with
75 eigenvalue-eigenvector based decomposition techniques to provide a unique solution to
76 discriminate scattering mechanisms. These decomposition methods have received con-
77 siderable attention over the last decade. Li et al. (2012) utilized the Freeman-Durden,
78 Cloude-Pottier, and the Touzi decomposition parameters to map and monitor rice
79 crops. The study showed that the decomposition parameters enhanced the ability to
80 monitor rice due to changes in the scattering phase centre with plant maturity. The
81 Freeman-Durden decomposition produced the highest classification accuracy (83%)
82 for rice identification, compared to the Touzi (82%) and the Cloude-Pottier (80%)
83 decompositions.

84 Lopez-Sanchez et al. (2014) investigated the differential variations of the scattering
85 power components from the Freeman-Durden decomposition with rice growth stages.
86 Unique signatures obtained from these scattering powers at each growth stages help

87 to identify rice phenology. However, the Freeman-Durden decomposition power com-
88 ponents are sensitive to the orientation of targets, and the volume scattering model
89 uses an ensemble of uniformly distributed dipoles. Therefore, this particular volume
90 model assumption may be seldom valid for all phenology stages for different crops.

91 Lopez-Sanchez, Ballester-Berman, and Hajnsek (2012), and Lopez-Sanchez, Cloude,
92 and Ballester-Berman (2012) investigated the importance of the dual co-polarized
93 TerraSAR-X data for monitoring rice phenological stages. The phase and correlation
94 between the two channels (HH and VV) provided valuable information with respect
95 to crop growth development. In their study, the Cloude α parameter from the dual co-
96 pol X-band SAR data showed significant sensitivity with rice development, where the
97 scattering mechanisms distinctly responded to phenological changes. Lopez-Sanchez,
98 Cloude, and Ballester-Berman (2012) introduced a model-based decomposition tech-
99 nique for dual co-polarimetric SAR data. The decomposition technique estimates a
100 random volume component plus a polarized contribution of the scattered wave (a
101 rank-1 mechanism). This technique provides useful polarimetric information on rice
102 morphology at different phenological stages.

103 In a separate study, Ullmann, Schmitt, and Jagdhuber (2016) proposed a two-
104 component decomposition technique for dual co-pol data. The approach is adapted
105 from the Yamaguchi decomposition. The data is decomposed into two scattering con-
106 tributions: surface and double-bounce under the assumption of a negligible vegetation
107 scattering component in the Tundra environment. Hence, this decomposition technique
108 might not provide adequate information for diffused, or the volume scattering compo-
109 nent for crops. In another study, Dey et al. (2020a) proposed unsupervised clustering
110 schemes for full and compact polarimetric SAR data using the target scattering-type
111 parameter (Dey et al. 2020). Their study utilized this scattering-type parameter along

with the scattering entropy to characterize different phenological stages of rice. The work highlighted the advantages of the novel clustering schemes for phenology classification for both full and compact polarimetric SAR data.

In the existing dual co-pol decomposition techniques proposed by Ullmann, Schmitt, and Jagdhuber (2016) and Lopez-Sanchez, Cloude, and Ballester-Berman (2012), the power components are either: (1) two polarized power components, or (2) a volume plus a polarized power component. Therefore, a target in an image can not be uniquely characterized using these techniques. In addition, none of these methods consider a measure of the degree of polarization of the scattered wave. The degree of polarization essentially indicates the total polarized scattered component from a target. Thus, it may provide additional information about the morphology of the target.

In this study, we propose a model-free scattering power decomposition framework uniformly for full-polarimetric (FP) and dual co-polarimetric (DP) SAR data. The technique utilizes information about the polarization state of the scattered wave in terms of the Barakat degree of polarization (Barakat 1977) and the Kennaugh matrix elements. Moreover, the scattering-type parameters for both FP and DP SAR data obtained from this technique are roll-invariant (i.e., independent of the target orientation angle about the radar line of sight).

We use these power components to classify different phenological stages of rice. The phenology classification accuracy is compared with scattering powers obtained from other existing decomposition techniques. In summary, this study focuses on:

- Proposal of a framework utilizing the Kennaugh matrix to describe the novel target scattering-type parameter from FP and DP SAR data.
- Utilization of this parameter in the proposal of a novel model-free 3 component scattering power decomposition for DP SAR data.

- Application of the scattering-type parameter and the power components for rice phenology classification.
- Comparison of the classification accuracy utilizing the DP parameters with FP SAR data.

2. Study area

The study area is located near the city of Vijayawada in the state of Andhra Pradesh, India ($16^{\circ}24'6.2''\text{N}$, $8^{\circ}41'2.4''\text{E}$) as shown in Figure 1 (Mandal et al. 2019). The climatic zone varies from sub-humid to humid within the study area, with mostly clayey soil texture in this region. The spatial coverage of this test site is $\approx 25 \text{ km} \times 25 \text{ km}$. Rice is a major crop grown in this area. Depending on the variety and cultivation practices, the sowing period of rice varies from mid-June to mid-July. However, in general, cultivation starts after the pre-monsoon rain and rice is harvested during mid-December. The average field size is $\approx 60 \text{ m} \times 60 \text{ m}$. In each field, two sampling locations were chosen for in-situ measurements. Information about the crop growth stage, management practices, and biophysical parameters was noted during a field campaign which was conducted from June to December 2019.

[Figure 1 about here.]

3. Satellite data sets and pre-processing

Fine Quad Wide (FQW) mode Radarsat-2 images were acquired from July to November 2019 over the test site, as shown in Table 1. These images were multilooked by a factor of 2×3 pixels in the range and azimuth directions, respectively, to generate $\approx 15 \text{ m} \times 15 \text{ m}$ square pixel images. During rice cultivation typically many adjacent

159 fields are cultivated together. Therefore, the region appears homogeneously cropped,
160 even though each individual parcel's size is small. Hence, a 3×3 boxcar filter (Lee
161 and Pottier 2009) was applied to reduce speckle. Dual co-polarimetric (DP) SAR data
162 (HH-VV) were extracted from the FP data and are subsequently co-registered with a
163 Root Mean Square Error (RMSE) ≤ 0.25 m.

164 [Table 1 about here.]

165 4. In situ measurement procedures

166 In this study, 40 in-situ field measurements were analyzed. Soil moisture was mea-
167 sured in each field for two sampling locations. These locations were arranged in two
168 parallel transects along the row direction, with a separation between each transect
169 of ≈ 40 m. Theta-probes were used to collect moisture measurements. The soil was
170 saturated during the majority of the season due to irrigation and rainfall events.
171 Vegetation measurements were gathered at two points in each field. The location
172 of these points was driven by the spatial heterogeneity of plant growth within the
173 fields. At each point, the Plant Area Index (PAI), plant height, and phenology
174 were measured using non-destructive methods. The PAI was determined using hemi-
175 spherical digital photography, with ten photos collected at each sample point along
176 two transects separated by 2 m. Photographs were taken using a wide-angle lens
177 mounted on a digital camera. All photos were post-processed using the CanEYE soft-
178 ware (<https://www6.paca.inra.fr/can-eye>), which calculates an estimate of the
179 PAI. Descriptions of distinct phenology stages of rice are shown in Table 2 and the
180 statistics of different bio-physical and soil parameters are given in Table 3.

181 [Table 2 about here.]

[Table 3 about here.]

The morphological developments of rice across its various phenological stages are shown in Figure 2. The growth stages of rice usually consist of three major phases: vegetative, reproductive, and maturity. In the test site, the cultivation time of rice depends mainly on rainfall events. The growing period of rice varies from 100 days to 140 days, depending on the varieties of rice. Short-duration cultivation lasts for 100-120 days, medium-duration for 120-140 days, and long-duration for almost 160 days (Adhikari et al. 2011). The vegetative phase begins with the germination of the seeds and ends with fully developed plants. In this period, the number of tillers increases and stems elongate. The germination phase consists of seed and radicle development. The onset of the first tiller defines the initiation of the tillering stage. During booting, the upper part of the stem becomes thick, and flag leaf development begins. During this period, the majority of plants remain vertical, known as the erectophile structure. Subsequently, panicle emergence and heading stages are observed. During this period, significant leaf inclination and increased random structures are visible. The fruit development stage starts when the grain appears and later becomes milky following the complete development of anthers. In the subsequent stage, dough followed by the ripening condition of rice leads to the final harvest. During the late-ripening period, the plant-water content drops, and rice appears to be dry. The fully grown structure of rice becomes random as grains become heavy, while the number of leaves decreases (Moldenhauer and Slaton 2001).

[Figure 2 about here.]

204 5. Methodology

205 In polarimetric SAR, the 2×2 complex scattering matrix \mathbf{S} contains complete polari-
 206 metric information about backscattering from targets for each pixel. It is expressed
 207 in the backscatter alignment (BSA) convention in the linear horizontal (H) and linear
 208 vertical (V) polarization basis as,

$$\mathbf{S} = \begin{bmatrix} S_{HH} & S_{HV} \\ S_{VH} & S_{VV} \end{bmatrix} \Rightarrow \mathbf{k} = V([\mathbf{S}]) = \frac{1}{2}\text{tr}(\mathbf{S}\Psi), \quad (1)$$

209 where $V(\cdot)$ is the vectorization operator on the scattering matrix, Ψ is the corre-
 210 sponding basis matrix, and tr is the sum of the diagonal elements of the matrix. Each
 211 element of the matrix represents the backscattering response of the target at a specific
 212 polarization. The matrix's diagonal elements represent the co-polarized scattering in-
 213 formation, while the off-diagonal terms represent the cross-polarized information. In
 214 the monostatic backscattering case, the reciprocity theorem constrains the scattering
 215 matrix to be symmetric (i.e., $S_{HV} = S_{VH}$).

The multi-looked Hermitian positive semi-definite 3×3 coherency matrix \mathbf{T} is ob-
 tained from the averaged outer product of the target vector \mathbf{k}_P (derived using the
 Pauli basis matrix, Ψ_P) with its conjugate (i.e., $\mathbf{T} = \langle \mathbf{k}_P \cdot \mathbf{k}_P^{*T} \rangle$). Similarly, the 3×3
 covariance matrix \mathbf{C} is obtained from the averaged outer product of the target vec-
 tor \mathbf{k}_L (derived using the Lexicographic basis matrix, Ψ_L) with its conjugate (i.e.,

$$\mathbf{C} = \langle \mathbf{k}_L \cdot \mathbf{k}_L^{*\text{T}} \rangle.$$

$$\Psi_P = \left\{ \sqrt{2} \begin{bmatrix} 1 & 0 \\ 0 & 1 \end{bmatrix} \quad \sqrt{2} \begin{bmatrix} 1 & 0 \\ 0 & -1 \end{bmatrix} \quad \sqrt{2} \begin{bmatrix} 0 & 1 \\ 1 & 0 \end{bmatrix} \right\}, \quad (2)$$

$$\Psi_L = \left\{ 2 \begin{bmatrix} 1 & 0 \\ 0 & 0 \end{bmatrix} \quad 2\sqrt{2} \begin{bmatrix} 0 & 1 \\ 0 & 0 \end{bmatrix} \quad 2 \begin{bmatrix} 0 & 0 \\ 0 & 1 \end{bmatrix} \right\}. \quad (3)$$

216 In this study, we utilize the 4×4 real Kennaugh matrix \mathbf{K} to describe backscattering
 217 that is expressed in terms of the elements of the \mathbf{T} matrix as,

$$k_{ij} = \frac{1}{2} \text{tr}(\mathbf{T} \eta_{4i+j}), \quad \text{where} \quad \eta_{4i+j} = (-1)^{(-\delta_{3j})} \mathbf{A} (\sigma_i \otimes \sigma_j) \mathbf{A}^{*\text{T}}, \quad (4)$$

218 where k_{ij} is an elements of \mathbf{K} , each σ_i is one of the four Pauli basis matrices and
 219 $*$ represents the complex conjugate. Here, η is a set of sixteen 4×4 matrices (the
 220 generators of the group $\text{SU}(4)$ plus the unit matrix) indexed by i and j as the elements
 221 of \mathbf{K} . These matrices represent a generalization of the Pauli matrices in \mathbb{C}^4 , i.e., the
 222 4-dimensional complex space (Cloude 1986). The 4×4 matrix formed from the four
 223 Pauli vectors is the unitary matrix \mathbf{A} given as,

$$\mathbf{A} = \frac{1}{\sqrt{2}} \begin{bmatrix} 1 & 0 & 0 & 1 \\ 1 & 0 & 0 & -1 \\ 0 & 1 & 1 & 0 \\ 0 & i & -i & 0 \end{bmatrix}, \quad \text{and} \quad \delta_{ij} = \begin{cases} 0 & i \neq j \\ 1 & i = j \end{cases} \quad (5)$$

224 where δ_{ij} is the Kronecker delta function indexed by i and j . Like the conventional
 225 degree of polarization (Born and Wolf 2013), the n D Barakat degree of polarization m_n

226 similarly characterizes the state of polarization (or purity) of an EM wave described
 227 by the $n \times n$ coherency matrix \mathbf{T} (Barakat 1977). The expression of m_n is given as,

$$m_n = \sqrt{1 - \frac{n^n |\mathbf{T}|}{\text{tr}^n(\mathbf{T})}}, \quad 0 \leq m_n \leq 1. \quad (6)$$

228 In this study, \mathbf{T} is either the 3×3 or the 2×2 coherency matrix for FP (HH|HV|VH|VV)
 229 or DP (HH|VV) SAR data, respectively. It can be shown that the Barakat degree of po-
 230 larization is linked to the polarimetric contribution of the Shannon entropy (Réfrégier
 231 et al. 2004). Here the subscript (or superscript) n denotes either FP or DP SAR data
 232 depending on the coherency matrix dimension.

233 In order to derive the scattering-type parameter θ_n from the FP or DP SAR data,
 234 let us first consider two free variables, η_1 and η_2 as,

$$\eta_1 = \tan^{-1} \left(\frac{k_{11} - k_{44}}{2 m_n k_{11}} \right) \quad \text{and} \quad \eta_2 = \tan^{-1} \left(\frac{k_{11} + k_{44}}{2 m_n k_{11}} \right), \quad (7)$$

235 where k_{11} and k_{44} are the elements of the Kennaugh matrix, \mathbf{K} . It may be noted,
 236 that $\frac{k_{11} - k_{44}}{2 m_n k_{11}}$ denotes the fraction of power scattered from the regular part of a
 237 target with respect to the total polarized power, and $\frac{k_{11} + k_{44}}{2 m_n k_{11}}$ denotes the fraction of
 238 scattered power from the irregular part of a target with respect to the total polarized
 239 power (Huynen 1970). Hence, by using a simple relationship, we obtain,

$$\begin{aligned} \tan \theta_n &= \tan(\eta_1 - \eta_2) \\ &= \frac{4 m_n k_{11} k_{44}}{k_{44}^2 - (1 + 4 m_n^2) k_{11}^2} \end{aligned} \quad (8)$$

240 where $k_{11} = (T_{11} + T_{22} + T_{33})/2$ and $k_{44} = (-T_{11} + T_{22} + T_{33})/2$ for FP SAR data,

241 and $k_{11} = (T_{11} + T_{22})/2$ and $k_{44} = (-T_{11} + T_{22})/2$ for DP SAR data. T_{ii} for $i = 1, 2, 3$
 242 are the diagonal elements of \mathbf{T} .

Utilizing $\theta_n \in [-45^\circ, 45^\circ]$, we split the polarized part of the total power, i.e., $2 m_n k_{11}$, into two components: even-bounce (P_d^n), and odd-bounce (P_s^n) scattering powers using a geometrical factor $(1 \pm \sin 2\theta_n)$. The diffused (i.e., depolarized) scattering power, (P_v^n) is obtained as the depolarized part of the total power:

$$P_d^n = m_n k_{11} (1 - \sin 2\theta_n), \quad (9)$$

$$P_v^n = 2 k_{11} (1 - m_n), \text{ and} \quad (10)$$

$$P_s^n = m_n k_{11} (1 + \sin 2\theta_n). \quad (11)$$

243 Variations of $(1 - \sin 2\theta_n)$ and $(1 + \sin 2\theta_n)$ for $\theta_n \in [-45^\circ, 45^\circ]$ is shown in Figure 3.
 244 The two extremes of θ_n are labelled as P_s and P_d . It can be noted from Figure 3(a)
 245 that for $(1 + \sin 2\theta_n)$: $P_s = 2.0$ and $P_d = 0.0$. These values indicate that $(1 + \sin 2\theta_n)$
 246 characterizes the odd-bounce scattering component. In contrast, it can be noted from
 247 Figure 3(b) that for $(1 - \sin 2\theta_n)$: $P_s = 0.0$ and $P_d = 2.0$. These values indicate that
 248 $(1 - \sin 2\theta_n)$ characterizes the even-bounce scattering component.

249 [Figure 3 about here.]

250 The following special cases are of particular interest:

251 **Complete depolarization:** $m_n = 0$, then $P_d^n = P_s^n = 0$, and $P_v^n = 2 k_{11}$.

252 **Pure even-bounce:** $m_n = 1$, and $\theta_n = -45^\circ$ with $P_s^n = P_v^n = 0$, and $P_d^n = 2 k_{11}$.

253 **Pure odd-bounce:** $m_n = 1$, and $\theta_n = 45^\circ$ with $P_d^n = P_v^n = 0$, and $P_s^n = 2 k_{11}$.

254 Therefore, the advantages of this proposed decomposition technique can be sum-
 255 marized as:

- 256 • The proposed decomposition technique is model-free, i.e., no prior assumption
257 on the type of scatterer existing within the scene is assumed. This is unlike the
258 conventional model-based decomposition techniques in the literature.
- 259 • It can be noted that the scattering-type parameter θ_n , along with the scattering
260 powers, P_d^n , P_s^n and P_v^n are roll-invariant (i.e., independent of target orientation
261 angle about the radar line of sight).
- 262 • The scattering power components are non-negative and the total power ($2 k_{11}$)
263 is conserved for any polarization state

264 For the sake of convenience, in the following text, we address the proposed FP decom-
265 position as MF3CF and the DP decomposition as MF3CD.

266 6. Results and Discussion

267 This section presents the temporal analysis for diverse rice growth stages using the
268 MF3CF and MF3CD decomposition parameters obtained from the Radarsat-2 full-
269 pol and extracted dual co-pol dataset. Figures 4 and 8 show the temporal variation
270 of θ_{FP} and θ_{DP} for different phenology stages of rice in this region. These values of
271 θ_{FP} and θ_{DP} , along with the scattering power components, are used for supervised
272 classification of rice phenological stages (as shown in Figures 7 and 11). We used the
273 bootstrap sampling procedure with 600 trees with a maximum depth of 10 trees for
274 classification using the random forest (RF) technique. The out of bag error starts
275 to saturate beyond 600 trees. Several studies reported in the literature (Lawrence,
276 Wood, and Sheley 2006; Dey et al. 2020b) confirms this fact. Tables 4 and 6 present
277 an analysis of the clustering accuracies. The confusion matrix for full pol is given in
278 Figures 6(a), 6(b), 6(c), 6(d), and for dual pol is given in Figures 10(a), 10(b), 10(c).

279 To compare the effectiveness of MF3CD's powers for classification, we first conduct
 280 its analysis with MF3CF's powers, proposed in Dey et al. (2020) for FP SAR data.

281 [Figure 4 about here.]

282 **6.1. Full-polarimetric SAR data**

283 Utilizing MF3CF, we compute the scattering-type parameter, θ_{FP} from the full-
 284 polarimetric C-band Radarsat-2 SAR data. The spatial variation of θ_{FP} as a function
 285 of rice phenology is shown in Figure 4. In total, 4 sample fields (F1, F2, F3 and F4)
 286 are used for the trend analysis of θ_{FP} (Figure 5). The temporal trend in θ_{FP} , P_d^{FP} ,
 287 P_s^{FP} and P_v^{FP} indicates phenological development of rice.

288 At the beginning of the cultivation season, most of the fields were bare and smooth.
 289 Hence, on 06 June 2019, θ_{FP} ranges between $[30^\circ, 40^\circ]$, which indicates odd-bounce
 290 scattering, with some variations due to differences in surface roughness in different
 291 fields.

292 The degree of polarization (m_{FP}) during this period is also high and varies between
 293 0.7 to 0.9. These high values are due to the fairly smooth field condition at this early
 294 stage. Hence, predominant odd-bounce scattering power is evident from Figure 5.
 295 Therefore, P_s^{FP} is the dominant scattering power that varies $\approx 70\%$ to 80% .

296 In contrast, P_d^{FP} and P_v^{FP} values are fairly low early in this season. These low values
 297 of the scattering power components obtained from MF3CF are due to the absence of
 298 crop structure and a high coherent scattering mechanism. However, an anomaly in
 299 the values of θ_{FP} , m_{FP} and P_s^{FP} is observed in field F3. The exception in the values
 300 of these two parameters might be due to the moderate roughness condition, which
 301 occurred due to ploughing.

302 On 24 July 2019, rice entered the early tillering stage. With the onset of rice mor-

303 phology, θ_{FP} begin to decrease. At this stage, the values of θ_{FP} are $\approx 15^\circ$ for most of
304 the fields. These low values of θ_{FP} are due to foliage growth, which must have slightly
305 increased randomness in the scattering phenomenon.

306 However, for field F2, it is observed that the value of θ_{FP} is $\approx 0^\circ$, i.e., the high
307 amount of randomness present in the scattered wave. Rice growth in this field was
308 more advanced. As a result the large number of tillers may explain this low value of
309 θ_{FP} . The PAI was around $0.9 \text{ m}^2 \text{ m}^{-2}$ during this active tillering stage.

310 The increase in scattering randomness further affects the overall polarization struc-
311 ture of the backscattered wave. The degree of polarization is lower as compared to 06
312 June 2019. During this period, m_{FP} varies between 0.6 to 0.8 depending on the growth
313 characteristics in different rice fields. Although the values of m_{FP} are low, the crops
314 were still sparsely distributed. Hence, the scattering from the water surface beneath
315 the crops was dominant during this period. As a consequence, this high backscatter
316 from the water surface leads to a dominant P_s^{FP} power component.

317 On the other hand, the interaction of the wave with crop stems and the water surface
318 generated a small increment in the P_d^{FP} power component. Besides, the amount of
319 diffused power component has also increased substantially due to the emergence and
320 development of the crops. During this period, the proportion of P_s^{FP} power was $\approx 60\%$,
321 while the proportion of P_d^{FP} and P_v^{FP} powers were $\approx 16\%$ and $\approx 24\%$, respectively.

322 θ_{FP} continues to decrease on 17 August 2019 when the majority of rice fields were
323 in their advanced tillering stage. At this stage, the values of θ_{FP} are $\approx -16^\circ$, which
324 indicates a change in the scattering mechanisms. This shift in the scattering mechanism
325 is mainly due to the emergence and development of rice plants. The appearance of even-
326 bounce scattering is due to the combined backscattering effect from the crop stem and
327 the underlying water surface.

[Figure 5 about here.]

During this period, the vertical structure of the crop and the underlying water jointly enhanced the degree of polarization of the scattered wave. However, differences in the trend of m_{FP} are observed among F1, F2, F3 and F4 fields. A slight increase in the values of m_{FP} is evident for F1 and F3 fields from Figure 5, while a decrease is observed for fields F2 and F4. The increase in m_{FP} for F1 and F3 fields is likely due to the development of prominent vertical crop structure. In contrast, the decrease for F2 and F4 fields might be due to the non-homogeneous growth of the plants, where some canopies were more advanced than others.

Rice was cultivated 4-6 days earlier in the F2 and F4 fields than the F1 and F3 fields. Hence, the canopy cover in fields F2 and F4 was higher relative to F1 and F3. Nevertheless, the crop growth in each field, except F2 has led to a dominance of P_d^{FP} power during scattering.

At this stage of development, the value of P_d^{FP} is $\approx 53\%$, while the value of P_v^{FP} is $\approx 26\%$. In field F2, the complex crop geometry might have produced a high amount of diffused power component. It is important to note that from the date onwards, P_v^{FP} shows an increasing trend for most fields.

The remaining phenological stages are dominated by even-bounce scattering, due to the interaction of the wave with stems and the water surface. This feature was earlier reported by Lopez-Sanchez et al. (2014) while analyzing Cloude alpha and the phase difference between the HH and VV channels.

During this period, some fields showed variations in θ_{FP} between -5° and 10° due to leaf and foliage development. These stems and leaves have increased scattering randomness, which is well characterized by θ_{FP} as multiple bounce effects.

Like 17 August 2019, a variation in the values of m_{FP} is observed depending upon

the crop morphological conditions. The complex structure of the leaves and foliage might have also increased the diffused power component, P_v^{FP} . However, the P_d^{FP} power is yet dominant due to the interaction of the electromagnetic wave with the stem and water.

In particular, significant multiple bounces are observed during the advanced reproductive stage of rice. At this time, the emergence of flowers contribute to a more random crop geometry. Hence, on 04 October 2019, θ_{FP} varies within $\approx [-14^\circ, 14^\circ]$. During this period, although the P_d^{FP} power is slightly higher than other power components, a shift in the dominancy between P_d^{FP} and P_v^{FP} powers begins during this stage of growth.

The amount of P_d^{FP} power is 40 % to 60 %, while the P_v^{FP} power is 20 % to 40 %. As the crop matures on 21 November 2019, θ_{FP} is centred on 0° . The dominance of P_v^{FP} power is evident for all fields, and m_{FP} decreases due to an increase in scattering randomness. θ_{FP} fluctuates around 0° , with the exception of field F4. During this period, most crop stems start to incline, although for some fields the crops remain vertical and the stem–water interaction generates a moderate amount of even-bounce power. At this time, the proportion of P_v^{FP} power is 40 % to 60 %, while P_d^{FP} and P_s^{FP} powers are $\approx 30\%$ and $\approx 20\%$, respectively.

We used these three scattering power components, P_s^{FP} , P_d^{FP} and P_v^{FP} to classify different phenological stages of rice with the multi-temporal C-band Radarsat-2 SAR dataset. In this analysis, we used the powers obtained from the An3D decomposition (An, Cui, and Yang 2010), F3D (Freeman and Durden 1998), Y3D (Yamaguchi 3-component decomposition) techniques and compared the classification with the powers obtained from the proposed FP method.

[Figure 6 about here.]

378 The phenology classification accuracies with the RF classifier are provided in Table 4
379 using the MF3CF, An3D, F3D and Y3D three-component full-polarimetric decom-
380 position techniques. We have particularly limited the classification comparison with
381 conventional three-component decomposition techniques since the proposed decompo-
382 sition technique generates only three scattering power components.

383 Table 5 details the global measures aggregated from Table 4. It can be noticed
384 from Table 4, that the producer’s accuracy (PA) for all bare fields using MF3CF
385 is 100 %. In contrast, the PA using F3D, Y3D and An3D are 85.41 %, 89.61 % and
386 79.17 %, respectively. This misclassification might be due to marginal confusion aris-
387 ing between bare field condition, early tillering and booting stages which is evident
388 from Figure 6(a), Figure 6(c) and Figure 6(b)). The assumptions of particular volume
389 models in the model-based decomposition techniques might have raised the marginal
390 confusion among the phenological stages. During this period, significant odd-bounce
391 and volume scattering power components might have increased the confusion among
392 these stages.

393 The user’s accuracy (UA) using MF3CF is slightly low (94.11 %). This indicates
394 that other phenology classes are misclassified as a bare field class (Figure 6(d)). As a
395 consequence, Figure 7 maps the majority of the fields as bare, while a few fields are
396 more phenologically advanced depending upon date of sowing.

397 [Table 4 about here.]

398 [Table 5 about here.]

399 During early and advanced tillering stages, the PA drops to 82.92 % and 86.11 %,
400 respectively. This decrease might be due to the similarity in the scattering mechanisms
401 and the power components between the early tillering stages and advanced tillering.

402 A similar reduction in PA is also evident for F3D, An3D and Y3D.

403 The similarity between scattering mechanisms and the corresponding power com-
404 ponents from the advanced tillering stage and the booting stage impacted the user's
405 and producer's accuracy, which is apparent in Figure 6(d). This effect is also ob-
406 served for other decomposition techniques in Figure 6(a), Figure 6(b) and Figure 6(c).
407 Consequently, misclassifications with other phenological stages were also evident (Fig-
408 ure 6(d)). This is indicated by the user's accuracy as shown in Table 4.

409 In contrast, the PA using the powers from the F3D, Y3D and An3D techniques for
410 early and advanced tillering stages are 78.04 %, 80.48 %, 80.48 %; and 69.44 %, 80.61 %, 91.67 %, respectively. As stated earlier, the confusion between the early tillering and
412 bare field condition is marginal for An3D and Y3D due to comparable scattering power
413 components. However for F3D, the confusion is higher between these two stages, as
414 well as between the advanced tillering and maturity stages. This could be due to
415 the high value of volume scattering computed by the F3D technique. For all these
416 three model-based decomposition techniques, the average reduction in UA and PA is
417 around 2 % and 7 %, respectively, as compared to bare field condition. It can be noted
418 that the differences between the PA of MF3CF and other techniques are marginal.
419 This small difference might be due to the advancement of crop growth which could
420 be partially accredited to the volume models assumed in those techniques. However,
421 based on different volume scattering models in those decomposition techniques, the
422 PA varies from one technique to another. For MF3CF, the P_v^{FP} component is due to
423 the depolarized component of the scattering wave. Hence, in this case, the power com-
424 ponents of MF3CF are able to capture the scattering characteristics from distributed
425 crop structures. As a consequence, the PA gets improved as compared to F3D, An3D
426 and Y3D.

427 An anomaly in the accuracy between MF3CF and An3D techniques is evident dur-
 428 ing the advanced tillering stages compared to the bare field and early tillering stages
 429 (Figure 6(b)). The PA and UA using the An3D technique are marginally higher than
 430 that of the proposed method. This anomaly might be due to the combination of P_d^{FP} ,
 431 P_s^{FP} and P_v^{FP} scattering power components in a unique manner. During this transi-
 432 tion period from an early tillering to the booting stage, the amount of polarized and
 433 depolarized power components generates uncertainty in the classification among early
 434 tillering, advanced tillering and booting stage using the proposed technique.

435 During the booting stage, the scattering signature from rice is majorly comparable
 436 to the advanced tillering stage as the crop attains a semi-rigid structure. Hence, the PA
 437 using MF3CF is 82.06 %, while the UA is 86.48 %. On the other hand, the PA for F3D,
 438 Y3D and An3D are 69.23 %, 79.92 % and 82.06 %, while the UA is 71.04 %, 76.92 %
 439 and 82.06 % respectively. It may be noted that during this period, the PA and UA for
 440 MF3CF and the F3D, Y3D, and An3D techniques are comparable, which could be due
 441 to similar scattering power components during this period. In particular, F3D, Y3D
 442 and An3D misclassify most of the booting stage crops as being in an advanced tillering
 443 stage because of the high volume scattering power computed by these methods during
 444 these two stages.

445 [Figure 7 about here.]

446 At the flowering stage, both PA and UA have increased as opposed to the booting
 447 stage. The PA and UA at this stage are 95.46 % and 95.47 % respectively using the
 448 MF3CF technique. In contrast, the PA and UA using the An3D method are 90.90 %
 449 and 93.02 %, using the F3D are 81.81 % and 87.80 %, and using the Y3D are 88.63 %
 450 and 90.69 %, respectively. This increase in the accuracies might be due to the devel-

451 opment of the anther in the rice. Most of the time, the flowering stage consists of
452 heading and flowering stages as flowering begins after a day heading stage completed.
453 Therefore, the fully visible panicle as well as the fully open flower which are ready to
454 shed pollen on each other for pollination makes this separable from booting and other
455 phenological stages.

456 During the maturity stage, both UA and PA records 100 % using MF3CF technique.
457 These accuracies at the maturity stage essentially indicate that the RF classifier has
458 had no confusion with other phenology stages. However, confusion of the maturity
459 stage with other advanced phenology stages is evident in Figure 6(a), Figure 6(b) and
460 Figure 6(c). Hence, a lower estimate of PA and UA are apparent during this stage.
461 These lower values might to due to the similarity in volume scattering components
462 during these stages.

463 Therefore, the above classification accuracy in terms of PA and UA states that
464 MF3CF decomposition parameters outperform the F3D, Y3D and An3D methods for
465 rice phenology classification. We also observe this difference in the accuracies in terms
466 of the overall accuracy and the kappa coefficient (κ).

467 The overall accuracy using MF3CF is 91.17 %, while the overall accuracy using the
468 F3D, Y3D and An3D methods are 76.89 %, 84.03 % and 82.77 %, respectively. Besides,
469 κ using the MF3CF is 0.91, whereas, it is 0.82 for the An3D, 0.73 for the F3D and
470 0.81 for the Y3D methods. Although the p -value for both methodologies affirms the
471 rejection of the null hypothesis, the p -value of MF3CF is much smaller than An3D, F3D
472 and Y3D. An analysis-ready temporal phenological map of rice is shown in Figure 7.
473 Therefore, the high κ and the p -value in Table 5 suggests that classification using
474 MF3CF holds excellent promise.

6.2. Dual co-polarimetric SAR data

This section utilizes the obtained target characterization parameters from the proposed MF3CD decomposition technique to classify rice phenological stages. To evaluate the performance of these scattering power components for rice phenology classification, we extracted the DP data from Radarsat-2 FP SAR data. The variations of θ_{DP} across all phenological stages of rice are shown in Figure 8. The variations of θ_{DP} , m_{DP} and MF3CD scattering power components, were considered for the same four rice fields, as used for the analysis of the FP data.

[Figure 8 about here.]

At the initial stages of crop development (i.e., early leaf development), scattering from the soil usually dominates. Hence, θ_{DP} is $\approx 30^\circ$ to 42° . The high values of θ_{DP} are due to the presence of co-polarized correlations with the absence of the cross-polarized component.

As discussed in the earlier section, some of the fields had a small amount of surfaces roughness. The overall θ_{DP} varies from 18° to 42° . However, due to the presence of moderately smooth to smooth soil surface in most of the fields, the percentage of polarized scattering power components has greatly increased.

In particular, the interaction of EM waves with soil is dominated by the single-bounce scattering type, and therefore, the surface scattering power increases during this period. m_{DP} ranges between 0.6 to 0.8, and the proportion of P_s^{DP} power ranges between 60 % to 80 %.

However, the P_v^{DP} power varies from field to field depending on the surface roughness. For example, $\approx 40\%$ of the diffused power component is apparent in a few fields where the soil surface condition was somewhat rough.

499 Tillering started on 24 July 2019, but the crop density was very low at this period,
500 and hence, the scattering from the soil surface was still dominant. However, crop
501 emergence has slightly increased scattering randomness. Consequently, the values of
502 θ_{DP} has decreased compared to 06 June 2019. During this period, it varies from 15°
503 to 30° .

504 Due to this increase in randomness, the values of m_{DP} has also decreased, and
505 it ranges from 0.5 to 0.6. These low values of m_{DP} influenced the scattering power
506 components significantly. During this period, the proportion of P_{s}^{DP} is similar to P_{v}^{DP} .
507 Besides, the amount of P_{d}^{DP} power has also increased due to the interaction of the EM
508 wave with the stem–water configuration.

509 [Figure 9 about here.]

510 At the advanced tillering stage on 17 Aug, θ_{DP} reveals a significant contribution
511 of the even-bounce scattering mechanism. As stated earlier, this increase in the even-
512 bounce scattering is due to the wave interaction among the rice stem and surface
513 water.

514 Even-bounce scattering mechanism is apparent throughout the flowering stage. Be-
515 sides, m_{DP} values decreased from 24 July 2019 to 17 August 2019. However, through-
516 out the phenology cycle, the cross-polarization component increases. Therefore, the
517 absence of this cross-polarization component has lowered the values of m_{DP} , in com-
518 parison to m_{FP} . The values of θ_{DP} and m_{DP} during these periods are -5° to 30° and
519 0.2 to 0.6.

520 Starting from the advanced tillering stage, P_{v}^{DP} powers prevails dominant. On 10
521 Sep, rice advanced to the booting stage. During this stage, values of m_{DP} have in-
522 creased compared to 17 August 2019, which might be due to the presence of a weak

523 cross-polarization component.

524 As a result, the magnitude of P_d^{DP} powers has increased as compared to the previous
525 date. A similar situation exists during the flowering stage on 04 Oct except for field
526 F2. During this time, P_v^{DP} and P_d^{DP} powers coexists with significant proportion. For
527 field F2, the P_v^{DP} power is considerably higher than other components, which is due
528 to high depolarization of the backscattered waves from this field.

529 During the maturity stage, multiple scattering from the canopy and soil is more
530 apparent. Hence, on 21 November 2019, θ_{DP} fluctuates from -8° to 10° . The multiple
531 scattering from the fields has increased the amount of depolarization in the backscat-
532 tered EM wave. m_{DP} varies in the range of 0.2 to 0.4. As a result, the magnitude of
533 P_v^{DP} is very high in each field. The values of P_v^{DP} ranges from 60 % to 80 %. Conversely,
534 the values of P_s^{DP} and P_d^{DP} are significantly lower than 20 %.

535 [Table 6 about here.]

536 [Table 7 about here.]

537 [Figure 10 about here.]

538 Here we have shown rice phenology classification using the MF3CD scattering pow-
539 ers: P_d^{DP} , P_s^{DP} and P_v^{DP} from dual co-polarimetric SAR data. Additionally, the phenol-
540 ogy classification accuracy is compared with the results obtained from FP SAR data.
541 The producer's and user's accuracies are provided in Table 6 along with the global
542 measurements in Table 7. We have also compared the proposed MF3CD technique's
543 classification accuracy with the existing decomposition technique for DP SAR data
544 proposed by Ullmann, Schmitt, and Jagdhuber (2016) (U2D). Additionally, the ele-
545 ments of the \mathbf{T}_2 coherency matrix (i.e. T_{11} , T_{22} and $|T_{12}|$) are also used for phenology
546 classification.

547 It can be noted from Table 6, that the PA and UA for bare field condition (BF) are
 548 identical at 95.83 %, which is similar to the classification accuracies using MF3CF for
 549 FP data. However, the PA of MF3CD has decreased by ≈ 5 %, which might be due
 550 to the changes in the degree of polarization because of the absence of cross-polarized
 551 component in the coherency elements. On the other hand, the PA for U2D and \mathbf{T}_2
 552 matrix elements are 87.80 % and 82.92 %, respectively, while the UAs are 97.29 % and
 553 97.14 %, respectively. Hence, high UA essentially indicates that some pixels from other
 554 phenological stages are classified as the BF stage. From the confusion matrix shown
 555 in Figure 10(b) and Figure 10(a) we can observe a mixing among early transplanted
 556 (ET) and BF stages. At this stage, this mixing might have increased the UA for these
 557 two techniques.

558 The PA and UA during the early tillering stage are 80.48 % and 91.67 %, respectively,
 559 which could be due to the increase in the structural complexity of the crop. Besides,
 560 we describe the low accuracy of the early tillering stage by addressing the relative
 561 similarity in the values of P_s^{DP} and P_v^{DP} for the bare field, advanced tillering and
 562 maturity stages. The difference between the accuracies of MF3CD and MF3CF are
 563 marginal, which is due to similar depolarization structure and co-pol response. At this
 564 stage, the difference between UA of MF3CF and MF3CD is ≈ 2 % and PA is ≈ 3 %.
 565 We also observe a similar decreasing trend in the accuracies for U2D and \mathbf{T}_2 . The
 566 PA and UA of U2D are 84.62 % and 80.49 % and PA and UA of \mathbf{T}_2 are 79.48 % and
 567 75.61 %, respectively. At the advanced tillering, booting, and maturity stages, a similar
 568 pattern in the scattered power components produces significant confusion among the
 569 stages (Figure 10(c)), thereby decreasing PA and UA. Besides, an exception in the
 570 accuracies using MF3CF and MF3CD is evident during the booting period. The UA
 571 and PA using MF3CD technique are marginally higher than the MF3CF technique.

572 However, the PA and UA for U2D and \mathbf{T}_2 are significantly lower during booting. This
573 difference might be due to inadequate information about the scattering from a target
574 acquired by DP SAR data.

575 [Figure 11 about here.]

576 During booting, the similar diffused power component creates confusion with the
577 advanced tillering stage. Besides, being short duration booting and flowering stages
578 arise alike polarimetric features in the co-pol response. However, coherence between
579 the co-polar channels still exhibits a unique pattern compared to other phenological
580 stages. This pattern might impact the scattering power components of the dual co-
581 polarimetric data, which depends only on the co-polar coherence term in the absence
582 of the cross-polar component. On the other hand, as discussed earlier, the flowering
583 stage shows a significant difference due to anther and fully visible heads. The presence
584 of these crop morphological features generates a difference in the scattering mecha-
585 nism, which increases the UA and PA at the flowering stage. The PA at the flowering
586 stage is 90.90 %, while UA is 93.02 %. Furthermore, ample diffused scattering power
587 component created considerable confusion during rice phenology classification in later
588 phenological stages. Similar increase is also evident for \mathbf{T}_2 elements and U2D de-
589 composition technique. The PA of \mathbf{T}_2 elements and U2D are 82.06 % and 82.04 %,
590 respectively, while UAs are 91.43 % and 91.43 %, respectively.

591 However, at the maturity stage, although the P_v^{DP} power is dominant, and the pat-
592 tern of P_d^{DP} and P_s^{DP} powers might have produced high PA (100 %) and UA (70.60 %).
593 In contrast, the absence of volume or diffused component in U2D and \mathbf{T}_2 elements has
594 lowered the PA and UA. The PA and UA for \mathbf{T}_2 elements are 64.86 % and 46.16 %,
595 respectively. The overall accuracy using MF3CD is 86.97 % with a κ of 0.84 (Table 7).

On the other hand, the overall classification accuracy using U2D and \mathbf{T}_2 elements are 76.47 % and 71.00 %, respectively. The analysis-ready map of rice phenology using MF3CD is shown in Figure 11. Therefore, it can be observed that the overall classification accuracy using our proposed MF3CD decomposition technique is comparable to FP data. These overall accuracy results infer the potential of employing our MF3CD decomposed scattering power components for rice phenology classification.

7. Conclusions

This study proposed a model-free scattering power decomposition framework for full-polarimetric (FP), and dual-polarimetric (DP) SAR data using the Kennaugh matrix elements $k_{ij} : i, j = 1, 2, 3, 4$. We used the k_{11} and k_{44} elements of the Kennaugh matrix and the n D Barakat degree of polarization to describe the scattering-type parameter. We then used the scattering-type parameter as a geometrical factor to compute the three scattering power components individually for full (MF3CF) and for dual co-pol (MF3CD) from the total scattered power. We utilized the full-pol (FP) and the extracted dual co-pol (DP) data from the C-band Radarsat-2 SAR data. The images were acquired through the entire expanse of rice development. The scattering power components vary with changes in rice phenology stages. The potential of these scattering power components was also assessed for characterizing rice growth condition.

The analysis of the results shows that the proposed scattering power components are sensitive to rice phenology and hence useful to classify different rice phenology stages. The power components can discriminate rice growth stages due to scattering purity changes based on the development of unique canopy structures as the season progresses. The overall classification accuracy using the proposed power components for the FP SAR data is better than the An and Yang three-component, Freeman and

620 Durden three-component, and Yamaguchi three-component decomposition techniques.
621 The overall accuracy using the proposed power components for the DP SAR data is
622 better than using only the matrix elements or the Ullmann two-component decom-
623 position technique. Moreover, the overall accuracy (OA) of using the proposed power
624 components for the DP SAR data is only marginally lower than the FP SAR data.
625 Like the FP SAR data, this study demonstrates the potential of DP SAR data for
626 efficient rice phenology classification. In this study the OA using MF3CF and MF3CD
627 are 91.17 % and 86.97 %, respectively.

628 Even though the results are quite encouraging, the study has some limitations based
629 on the available data sets. On the one hand, a denser time series of SAR data might
630 have reduced confusion between certain phenological stages, particularly booting and
631 flowering. In addition to this, enhancing the classification algorithm might also im-
632 prove the mapping of intermediate phenological stages. Further, dense temporal data
633 throughout the season can assist better cultivation practices. Besides this, short revisit
634 times are useful to monitor phenology information closely.

635 On the other hand, the proposed decomposition technique is model-free. Therefore,
636 the scattering power components are unique and unambiguous. Within the decom-
637 position framework, the target characterization parameters and the scattering power
638 components are roll-invariant. However, the proposed technique has a limitation based
639 on the nature of the coherency matrix for dual co-pol SAR data. It is apparent that the
640 framework can not be extended to obtain the target asymmetry component either in
641 terms of the scattering power components or the target characterization parameters.
642 Nevertheless, all the scattering power components of MF3CF and MF3CD are non-
643 negative and stable (i.e., the scattering power components does not change abruptly
644 with a small perturbation of the coherency matrix).

645 Please note that in this work, the studies were conducted in a semi-arid region.
646 However, the cultivation and management practice of rice could differ around the
647 globe. Therefore, one must expand this method for other sites and other types of
648 crops. Future studies should also include radar images acquired at X- and L-band,
649 such as the TerraSAR-X and ALOS-2 satellites. At high frequencies, X-band could
650 discriminate the initial growth stages from advanced growth stages. However, at lower
651 frequencies, we expect less sensitivity to the initial emergence of the plants, and,
652 as such, L-band might be useful to discriminate more advanced phenology stages of
653 crops. These multi-frequency analyses would lead to a better understanding of crop
654 phenology to the farming user community.

655 **Reproducibility and Replicability**

656 Following the guidelines presented in Frery, Gomez, and Medeiros (2020), we made
657 available the code that supports the reproducibility and replicability of this work in a
658 Github repository: <https://github.com/Subho07/MF3CD>.

659 **Acknowledgements**

660 This work was supported in part by the Spanish Ministry of Science, Innovation
661 and Universities, the State Agency of Research (AEI), and the European Funds for
662 Regional Development (EFRD) under Project TEC2017-85244-C2-1-P. The authors
663 would like to thank the Canadian Space Agency and MAXAR Technologies Ltd. (for-
664 merly MDA) for providing Radarsat-2 images through the Joint Experiment for Crop
665 Assessment and Monitoring (JECAM) SAR Inter-comparison Experiment network.
666 The authors are also thankful to Andhra Pradesh Space Application Centre (AP-

667 SAC), ITE & C Department, Government of Andhra Pradesh for their support during
668 field campaigns.

669 Disclosure statement

670 No potential conflict of interest was reported by the authors.

671 References

- 672 Adhikari, B, MK Bag, MK Bhowmick, and C Kundu. 2011. "Status paper on rice in West
673 Bengal." *Rice Knowledge Management Portal* <http://www.rkmp.co.in>.
- 674 An, W., Y. Cui, and J. Yang. 2010. "Three-Component Model-Based Decomposition for Po-
675 larimetric SAR Data." *IEEE Transactions on Geoscience and Remote Sensing* 48 (6): 2732–
676 2739.
- 677 Barakat, Richard. 1977. "Degree of polarization and the principal idempotents of the coherency
678 matrix." *Optics Communications* 23 (2): 147–150.
- 679 Born, Max, and Emil Wolf. 2013. *Principles of optics: electromagnetic theory of propagation,*
680 *interference and diffraction of light*. Elsevier.
- 681 Bouvet, Alexandre, Thuy Le Toan, and Nguyen Lam-Dao. 2009. "Monitoring of the rice crop-
682 ping system in the Mekong Delta using ENVISAT/ASAR dual polarization data." *IEEE*
683 *Transactions on Geoscience and Remote Sensing* 47 (2): 517–526.
- 684 Cloude, S. 1986. "Group theory and polarisation algebra." *Optik* 75: 26–36.
- 685 Cloude, Shane R, and Eric Pottier. 1997. "An entropy based classification scheme for land
686 applications of polarimetric SAR." *IEEE Transactions on Geoscience and Remote Sensing*
687 35 (1): 68–78.
- 688 Corcione, V, F Nunziata, L Mascolo, and M Migliaccio. 2016. "A study of the use of COSMO-
689 SkyMed SAR PingPong polarimetric mode for rice growth monitoring." *International Jour-*
690 *nal of Remote Sensing* 37 (3): 633–647.

691 De Bernardis, Caleb G, Fernando Vicente-Guijalba, Tomas Martinez-Marin, and Juan M
692 Lopez-Sanchez. 2015. "Estimation of key dates and stages in rice crops using dual-
693 polarization SAR time series and a particle filtering approach." *IEEE Journal of Selected*
694 *Topics in Applied Earth Observations and Remote Sensing* 8 (3): 1008–1018.

695 Dey, S., A. Bhattacharya, D. Ratha, D. Mandal, and A. C. Frery. 2020. "Target Characteriza-
696 tion and Scattering Power Decomposition for Full and Compact Polarimetric SAR Data."
697 *IEEE Transactions on Geoscience and Remote Sensing* 1–18.

698 Dey, Subhadip, Avik Bhattacharya, Debanshu Ratha, Dipankar Mandal, Heather McNairn,
699 Juan M. Lopez-Sanchez, and Y.S. Rao. 2020a. "Novel clustering schemes for full and compact
700 polarimetric SAR data: An application for rice phenology characterization." *ISPRS Journal*
701 *of Photogrammetry and Remote Sensing* 169: 135 – 151.

702 Dey, Subhadip, Dipankar Mandal, Laura Dingle Robertson, Biplab Banerjee, Vineet Kumar,
703 Heather McNairn, Avik Bhattacharya, and YS Rao. 2020b. "In-season crop classification us-
704 ing elements of the Kennaugh matrix derived from polarimetric RADARSAT-2 SAR data."
705 *International Journal of Applied Earth Observation and Geoinformation* 88: 102059.

706 Erten, Esra, Juan M Lopez-Sanchez, Onur Yuzugullu, and Irena Hajnsek. 2016. "Retrieval of
707 agricultural crop height from space: A comparison of SAR techniques." *Remote Sensing of*
708 *Environment* 187: 130–144.

709 Freeman, Anthony, and Stephen L Durden. 1998. "A three-component scattering model for
710 polarimetric SAR data." *IEEE Transactions on Geoscience and Remote Sensing* 36 (3):
711 963–973.

712 Frery, A. C., L. Gomez, and A. C. Medeiros. 2020. "A Badging System for Reproducibility
713 and Replicability in Remote Sensing Research." *IEEE J. Sel. Topics Appl. Earth Observ.*
714 *Remote Sens.* 13: 4988–4995.

715 Huynen, J R. 1970. "Phenomenological theory of radar targets." PhD dissertation, Technical
716 Univ., Delf, The Netherlands.

717 Koay, Jun-Yi, Chue-Poh Tan, Ka-Sing Lim, Saiful Bahari bin Abu Bakar, Hong-Tat Ewe, Hean-

718 Teik Chuah, and Jin-Au Kong. 2007. "Paddy fields as electrically dense media: Theoretical
719 modeling and measurement comparisons." *IEEE Transactions on Geoscience and Remote*
720 *Sensing* 45 (9): 2837–2849.

721 Koppe, Wolfgang, Martin L Gnyp, Christoph Hütt, Yinkun Yao, Yuxin Miao, Xiping Chen,
722 and Georg Bareth. 2013. "Rice monitoring with multi-temporal and dual-polarimetric
723 TerraSAR-X data." *International Journal of Applied Earth Observation and Geoinforma-*
724 *tion* 21: 568–576.

725 Küçük, Çağlar, Gülşen Taşkın, and Esra Erten. 2016. "Paddy-rice phenology classification
726 based on machine-learning methods using multitemporal co-polar X-band SAR images."
727 *IEEE Journal of Selected Topics in Applied Earth Observations and Remote Sensing* 9 (6):
728 2509–2519.

729 Kurosu, Takashi, Masaharu Fujita, and Kazuo Chiba. 1995. "Monitoring of rice crop growth
730 from space using the ERS-1 C-band SAR." *IEEE Transactions on Geoscience and Remote*
731 *Sensing* 33 (4): 1092–1096.

732 Lampayan, RM, JE Faronilo, TP Tuong, AJ Espiritu, JL De Dios, RS Bayot, CS Bueno, and
733 Y Hosen. 2015. "Effects of seedbed management and delayed transplanting of rice seedlings
734 on crop performance, grain yield, and water productivity." *Field Crops Research* 183: 303–
735 314.

736 Lawrence, Rick L, Shana D Wood, and Roger L Sheley. 2006. "Mapping invasive plants using
737 hyperspectral imagery and Breiman Cutler classifications (RandomForest)." *Remote Sensing*
738 *of Environment* 100 (3): 356–362.

739 Le Toan, Thuy, Henri Laur, Eric Mougin, and Armando Lopes. 1989. "Multitemporal and
740 dual-polarization observations of agricultural vegetation covers by X-band SAR images."
741 *IEEE Transactions on Geoscience and Remote Sensing* 27 (6): 709–718.

742 Le Toan, Thuy, Florence Ribbes, Li-Fang Wang, Nicolas Floury, Kung-Hau Ding, Jin Au Kong,
743 Masaharu Fujita, and Takashi Kurosu. 1997. "Rice crop mapping and monitoring using ERS-
744 1 data based on experiment and modeling results." *IEEE Transactions on Geoscience and*

745 *Remote Sensing* 35 (1): 41–56.

746 Lee, Jong-Sen, and Eric Pottier. 2009. *Polarimetric radar imaging: from basics to applications*.
747 CRC press.

748 Li, Kun, Brian Brisco, Shao Yun, and Ridha Touzi. 2012. “Polarimetric decomposition with
749 RADARSAT-2 for rice mapping and monitoring.” *Canadian Journal of Remote Sensing* 38
750 (2): 169–179.

751 Lopez-Sanchez, J. M., S. R. Cloude, and J. D. Ballester-Berman. 2012. “Rice Phenology Mon-
752 itoring by Means of SAR Polarimetry at X-Band.” *IEEE Transactions on Geoscience and*
753 *Remote Sensing* 50 (7): 2695–2709.

754 Lopez-Sanchez, Juan M, J David Ballester-Berman, and Irena Hajnsek. 2012. “First results of
755 rice monitoring practices in Spain by means of time series of TerraSAR-X dual-pol images.”
756 *IEEE Journal of Selected Topics in applied earth observations and remote sensing* 4 (2):
757 412–422.

758 Lopez-Sanchez, Juan M, Fernando Vicente-Guijalba, J David Ballester-Berman, and Shane R
759 Cloude. 2014. “Polarimetric response of rice fields at C-band: Analysis and phenology re-
760 trieval.” *IEEE Transactions on Geoscience and Remote Sensing* 52 (5): 2977–2993.

761 Mahajan, Gulshan, TS Bharaj, and J Timsina. 2009. “Yield and water productivity of rice
762 as affected by time of transplanting in Punjab, India.” *Agricultural Water Management* 96
763 (3): 525–532.

764 Mandal, D, V Kumar, YS Rao, A Bhattacharya, and KV Ramana. 2019. *Experimental Field*
765 *Campaigns at Vijayawada Test Site*. Technical Report MRS2019TR02. Microwave Remote
766 Sensing Lab, India. <http://doi.org/10.17605/OSF.IO/DN3E8>.

767 Moldenhauer, KEWC, and Nathan Slaton. 2001. “Rice growth and development.” *Rice pro-*
768 *duction handbook* 192: 7–14.

769 Réfrégier, Philippe, François Goudail, Pierre Chavel, and Ari Friberg. 2004. “Entropy of par-
770 tially polarized light and application to statistical processing techniques.” *JOSA A* 21 (11):
771 2124–2134.

- 772 Tian, Haifeng, Mingquan Wu, Li Wang, and Zheng Niu. 2018. "Mapping early, middle and late
773 rice extent using Sentinel-1A and Landsat-8 data in the Poyang lake plain, China." *Sensors*
774 18 (1): 185.
- 775 Torbick, Nathan, Diya Chowdhury, William Salas, and Jiaguo Qi. 2017. "Monitoring rice
776 agriculture across Myanmar using time series Sentinel-1 assisted by Landsat-8 and PALSAR-
777 2." *Remote Sensing* 9 (2): 119.
- 778 Touzi, Ridha. 2006. "Target scattering decomposition in terms of roll-invariant target param-
779 eters." *IEEE Transactions on Geoscience and Remote Sensing* 45 (1): 73–84.
- 780 Ullmann, Tobias, Andreas Schmitt, and Thomas Jagdhuber. 2016. "Two component decom-
781 position of dual polarimetric HH/VV SAR data: Case study for the tundra environment of
782 the Mackenzie Delta region, Canada." *Remote Sensing* 8 (12): 1027.
- 783 Yamaguchi, Y., A. Sato, W-M Boerner, R. Sato, and H. Yamada. 2011. "Four-Component
784 Scattering Power Decomposition With Rotation of Coherency Matrix." *IEEE Trans. Geosci.*
785 *Remote Sens.* 49 (6): 2251–2258.
- 786 Yang, Zhi, Yun Shao, Kun Li, Qingbo Liu, Long Liu, and Brian Brisco. 2017. "An improved
787 scheme for rice phenology estimation based on time-series multispectral HJ-1A/B and po-
788 larimetric RADARSAT-2 data." *Remote Sensing of Environment* 195: 184–201.
- 789 Yuzugullu, Onur, Esra Erten, and Irena Hajnsek. 2015. "Rice growth monitoring by means of
790 X-band co-polar SAR: Feature clustering and BBCH scale." *IEEE Geoscience and Remote*
791 *Sensing Letters* 12 (6): 1218–1222.
- 792 Zhang, Yuan, Xiaohui Liu, Shiliang Su, and Cuizhen Wang. 2014. "Retrieving canopy height
793 and density of paddy rice from Radarsat-2 images with a canopy scattering model." *Inter-*
794 *national Journal of Applied Earth Observation and Geoinformation* 28: 170–180.

795 List of Figures

796	1	Pauli RGB image acquired on 24 July, 2019 over the JECAM test site	
797		over Vijayawada, India. Region 1 and region 2 are the example subsets	
798		of sampling locations within the study area. The yellow box indicates	
799		the area over which the classification of rice phenology is performed. .	37
800	2	Crop morphological characteristics across phenological stages	38
801	3	Variation of (a) $1 + \sin 2\theta_n$ and (b) $1 - \sin 2\theta_n$ for $\theta_n \in [-45^\circ, 45^\circ]$. . .	39
802	4	Variation in θ_{FP} through the rice season with in the extent marked in	
803		yellow colour in Figure 1	40
804	5	Variation of m_{FP} , θ_{FP} and MF3CF scattering power components over	
805		the rice growing seasons	41
806	6	The confusion matrices (in %) among different phenological stages	
807		of rice (BF: Bare field, ET: Early tillering, AT: Advanced tillering,	
808		B: Booting, F: Flowering, M: Maturity).	42
809	7	Variations in clusters using the MF3CF scattering power components	
810		for the rice growing season with in the extent marked in yellow colour	
811		in Figure 1	43
812	8	Variation in θ_{DP} through the rice season with in the extent marked in	
813		yellow colour in Figure 1	44
814	9	Variation of m_{DP} , θ_{DP} and MF3CD scattering power components over	
815		the rice growing season	45
816	10	The confusion matrices (in %) among different phenological stages	
817		of rice (BF: Bare field, ET: Early tillering, AT: Advanced tillering,	
818		B: Booting, F: Flowering, M: Maturity)	46

819	11	Variation of cluster using MF3CD scattering power components for the	
820		rice growing season with in the extent marked in yellow colour in Figure 1	47

821 List of Tables

822	1	Radarsat-2 data acquired for the Indian test site	48
823	2	Description of rice morphology at different growth stages	49
824	3	Statistics (mean \pm standard deviation) of bio-physical and soil param-	
825		eters at different phenology stages of rice. Here, PH: plant height, PAI:	
826		plant area index, SM: soil moisture and NA: No measurements available	50
827	4	Producer's and User's accuracy of phenology stages of rice for MF3CF,	
828		An3D, F3D and Y3D decomposed power components using a RF classi-	
829		fier. BF: Bare field, ET: Early tillering, AT: Advanced tillering, B: Boot-	
830		ing, F: Flowering, M: Maturity, PA: Producer's accuracy, UA: User's	
831		accuracy	51
832	5	Global Measures for FP decomposition techniques	52
833	6	Producer's and User's accuracy of phenology stages of rice for MF3CD,	
834		U2D and \mathbf{T}_2 matrix elements using a RF classifier. BF: Bare field,	
835		ET: Early tillering, AT: Advanced tillering, B: Booting, F: Flowering,	
836		M: Maturity, PA: Producer's accuracy, UA: User's accuracy. The results	
837		are separately compared with MF3CF.	53
838	7	Global Measures for DP decomposition techniques	54

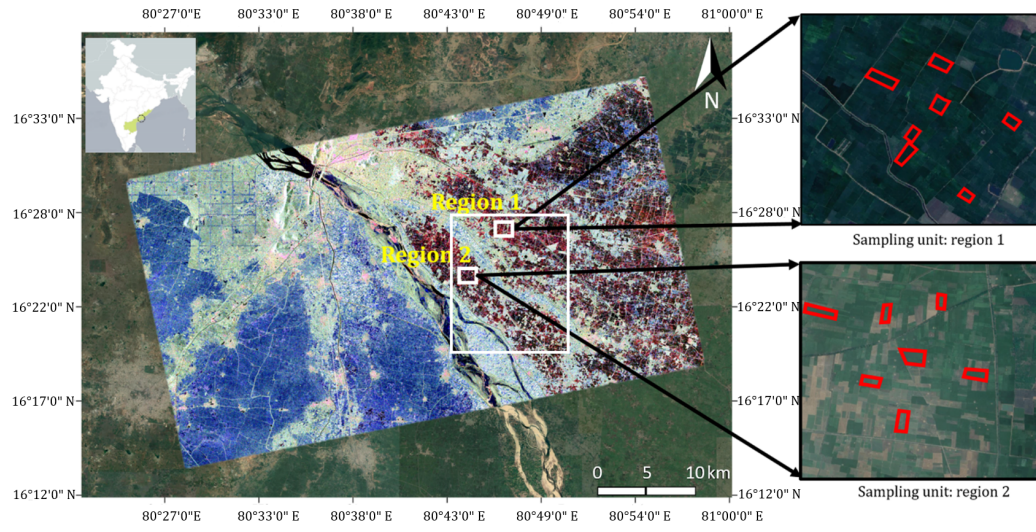


Figure 1. Pauli RGB image acquired on 24 July, 2019 over the JECAM test site over Vijayawada, India. Region 1 and region 2 are the **example subsets** of sampling locations within the study area. The yellow box indicates the area over which the classification of rice phenology is performed.

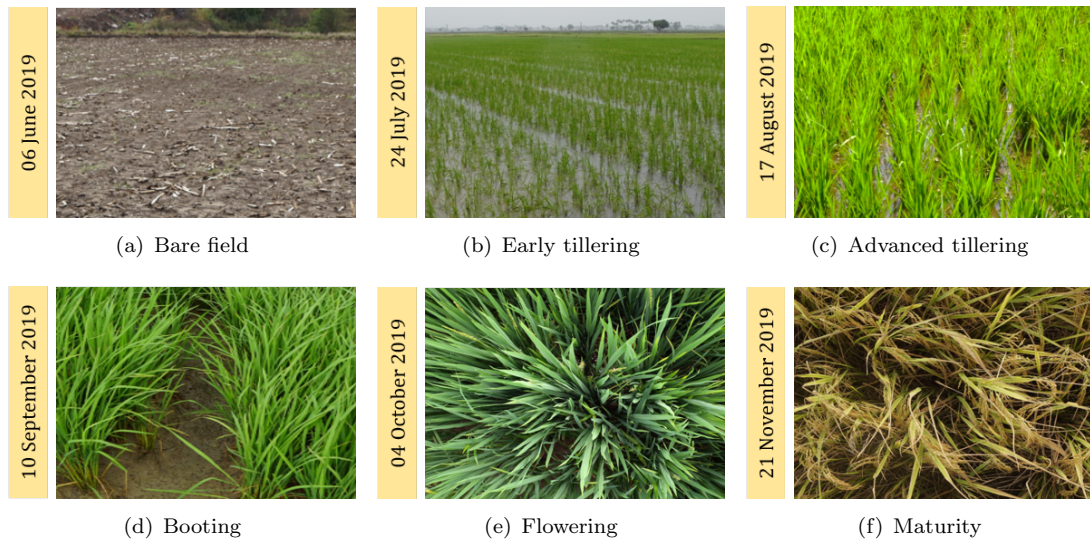


Figure 2. Crop morphological characteristics across phenological stages

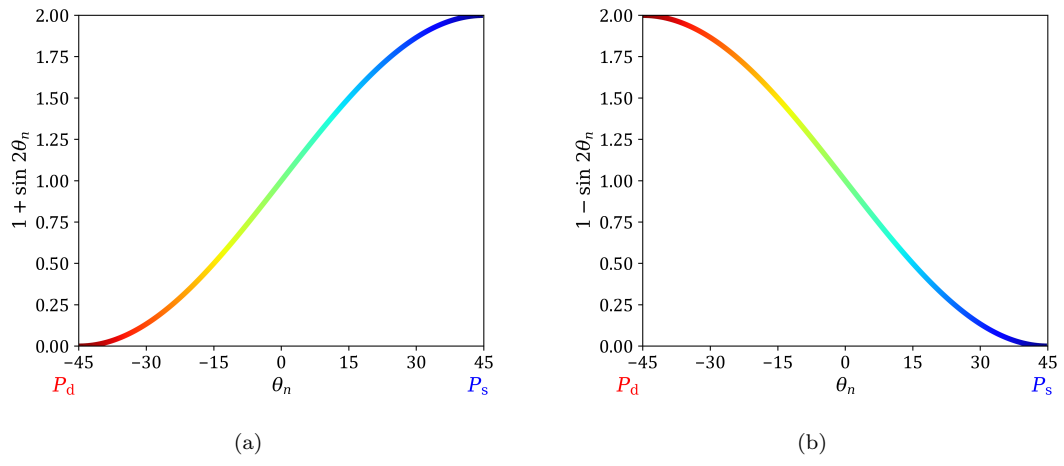


Figure 3. Variation of (a) $1 + \sin 2\theta_n$ and (b) $1 - \sin 2\theta_n$ for $\theta_n \in [-45^\circ, 45^\circ]$.

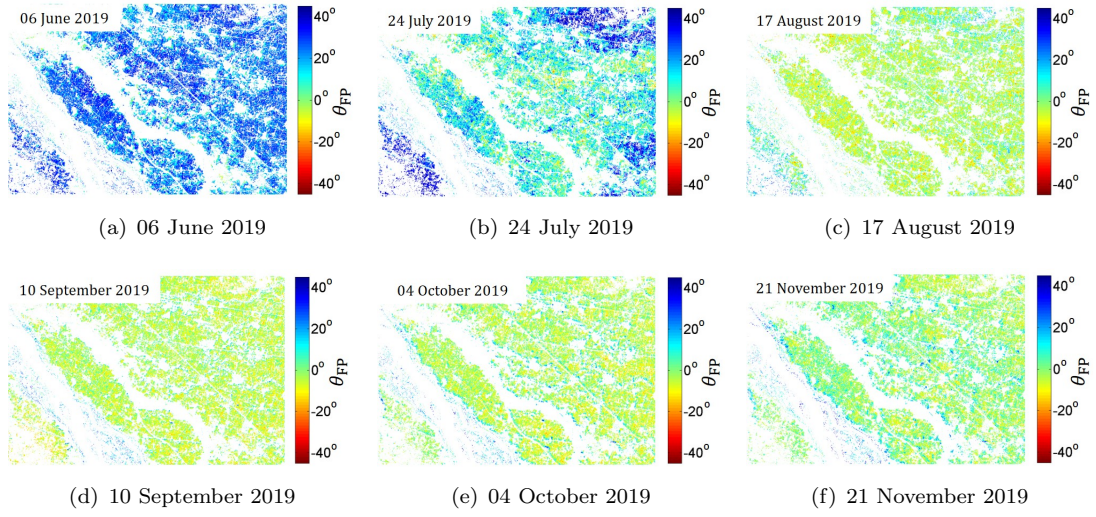


Figure 4. Variation in θ_{FP} through the rice season with in the extent marked in yellow colour in Figure 1

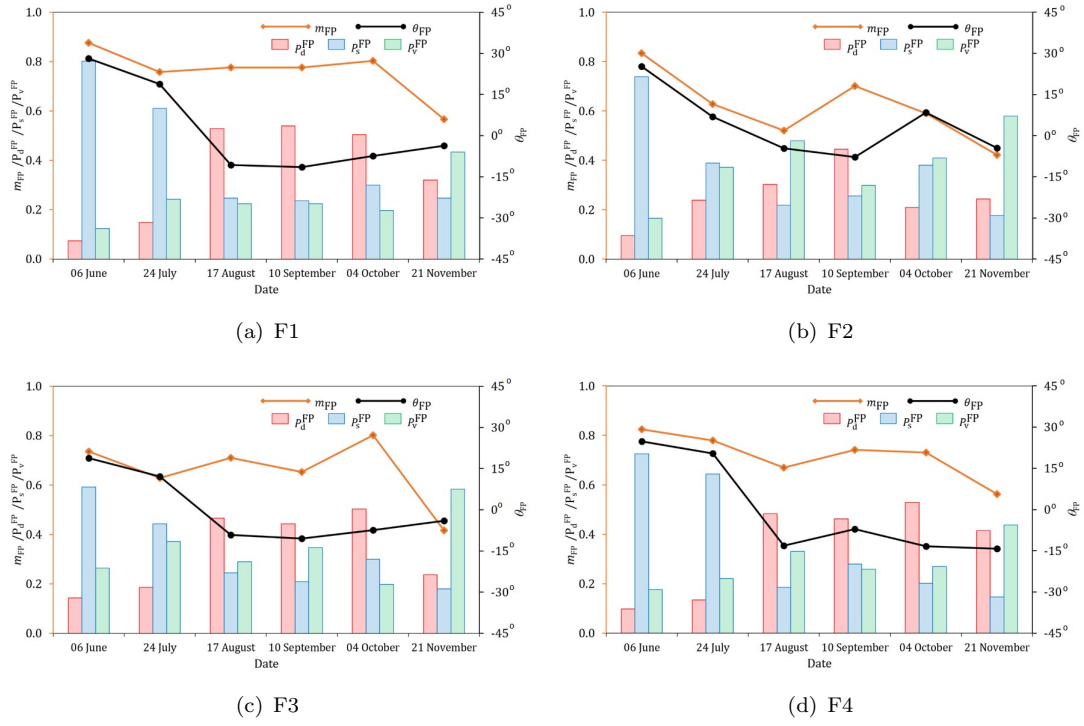


Figure 5. Variation of m_{FP} , θ_{FP} and MF3CF scattering power components over the rice growing seasons

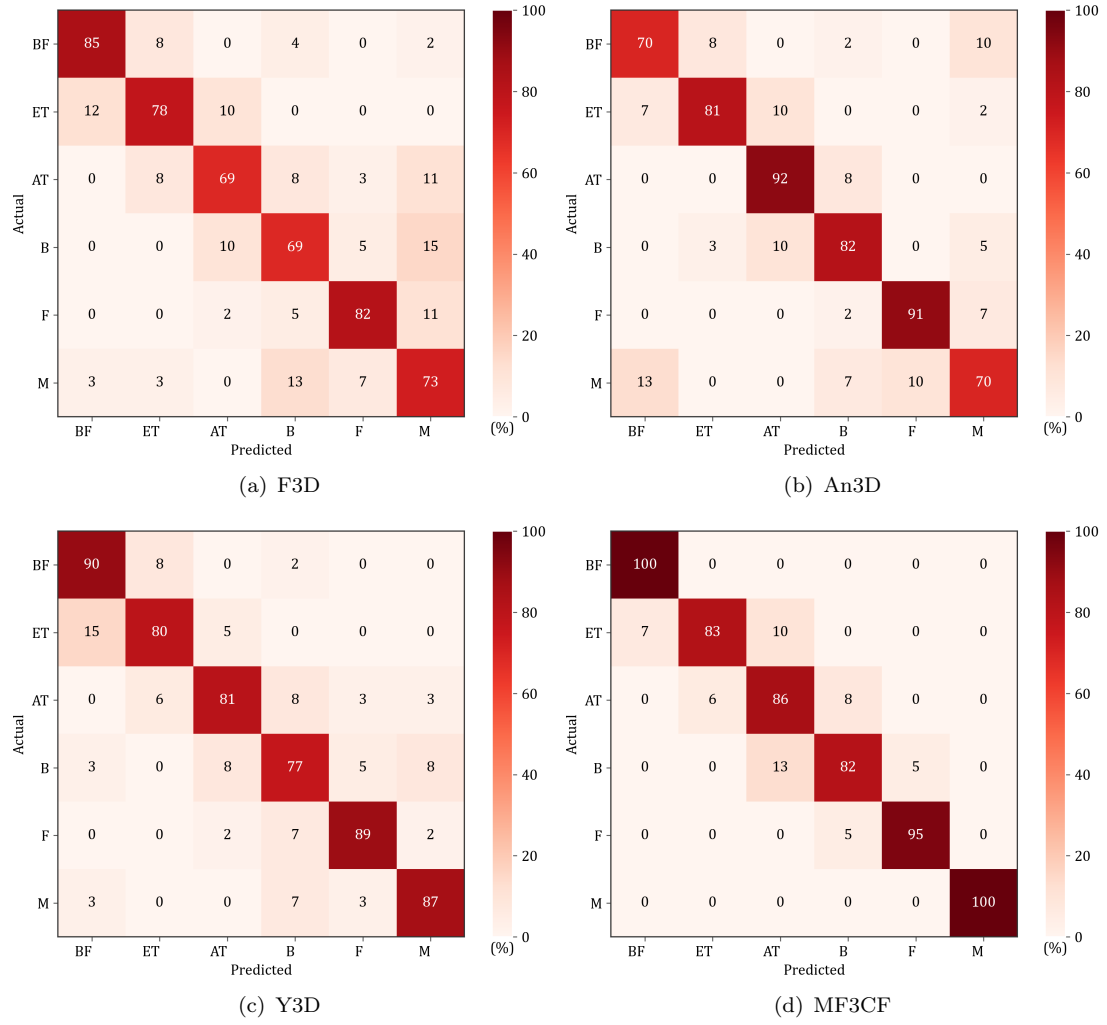


Figure 6. The confusion matrices (in %) among different phenological stages of rice (BF: Bare field, ET: Early tillering, AT: Advanced tillering, B: Booting, F: Flowering, M: Maturity).

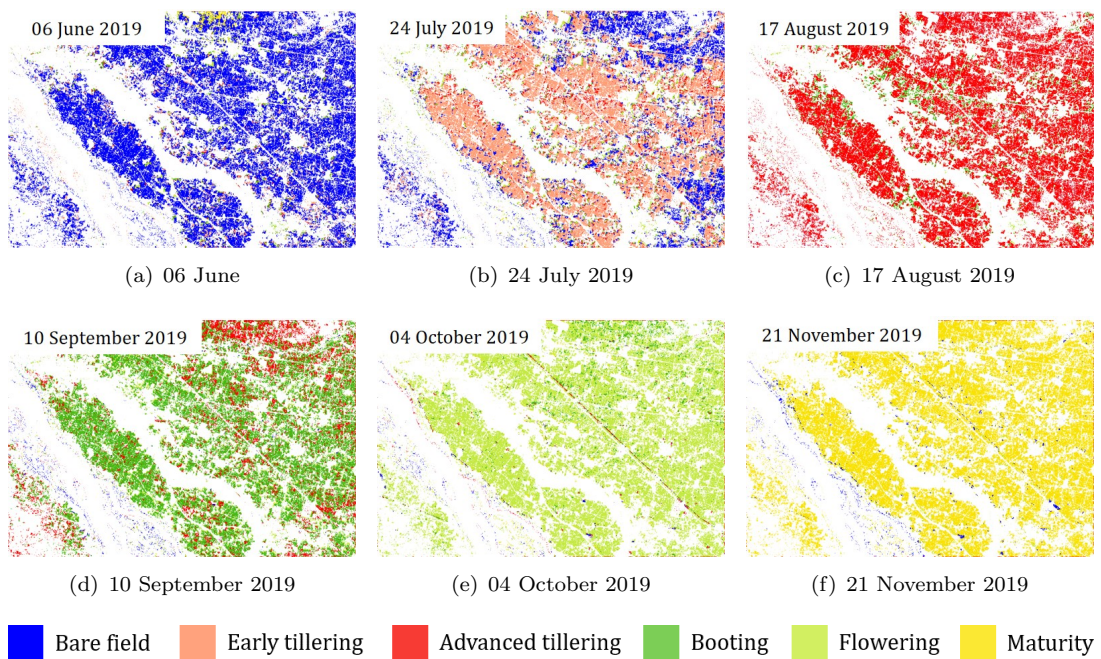


Figure 7. Variations in clusters using the MF3CF scattering power components for the rice growing season with in the extent marked in yellow colour in Figure 1

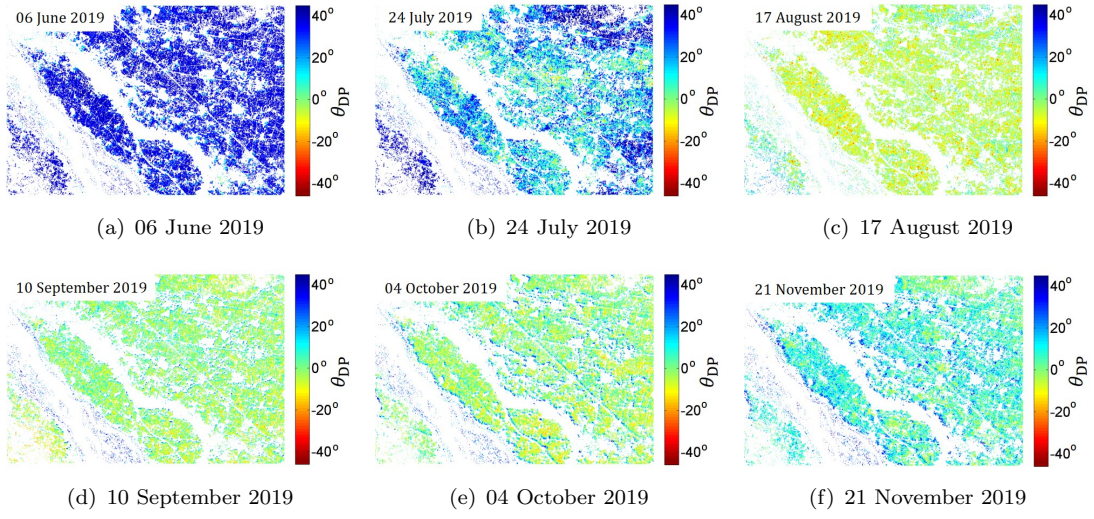


Figure 8. Variation in θ_{DP} through the rice season with in the extent marked in yellow colour in Figure 1

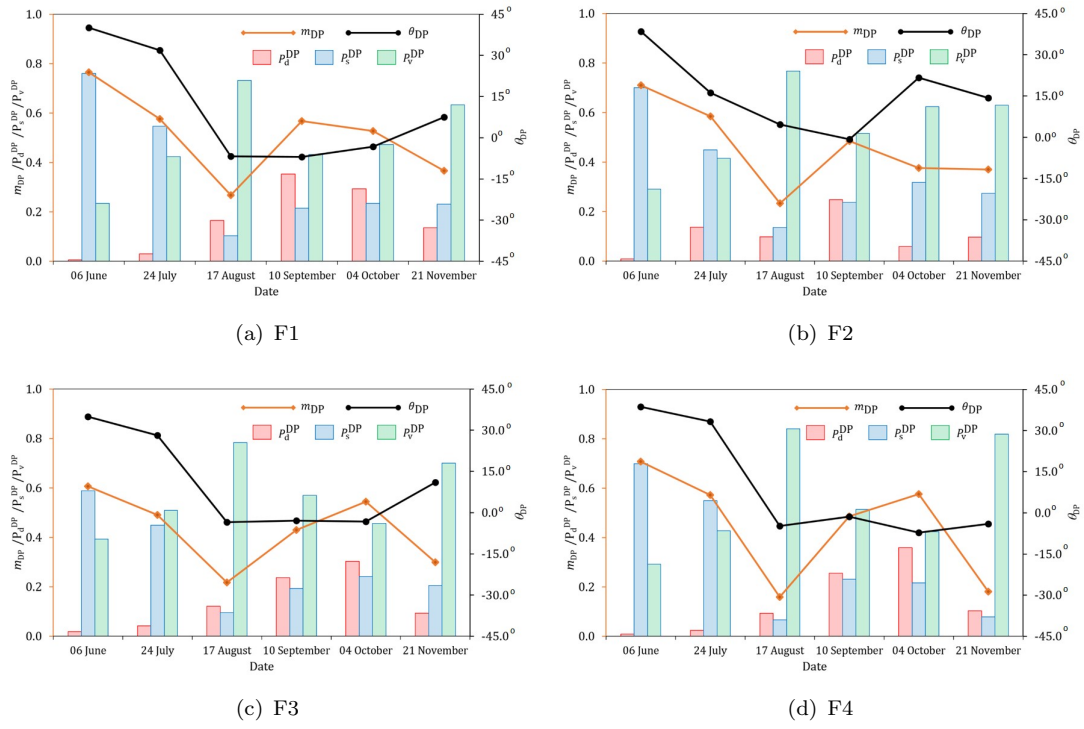


Figure 9. Variation of m_{DP} , θ_{DP} and MF3CD scattering power components over the rice growing season

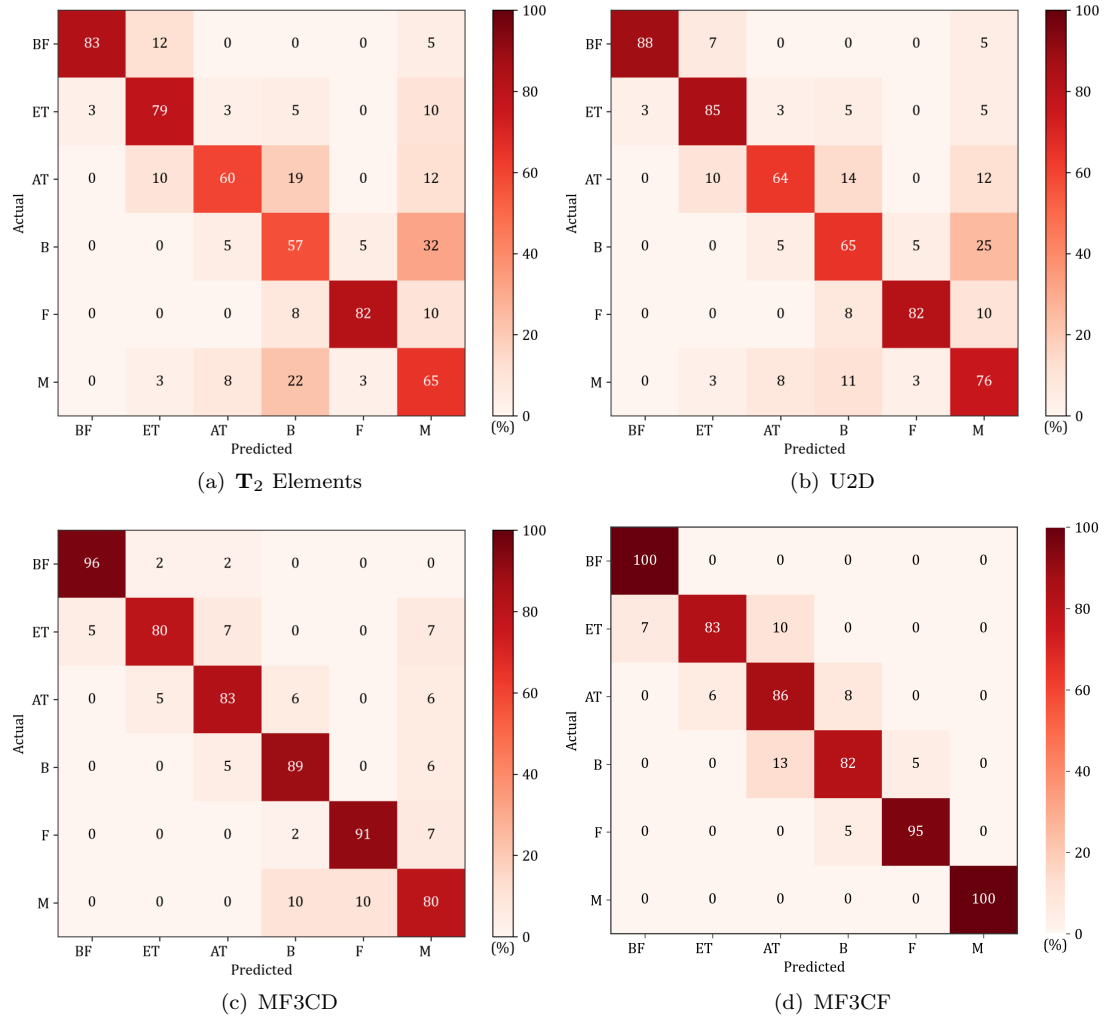


Figure 10. The confusion matrices (in %) among different phenological stages of rice (BF: Bare field, ET: Early tillering, AT: Advanced tillering, B: Booting, F: Flowering, M: Maturity)

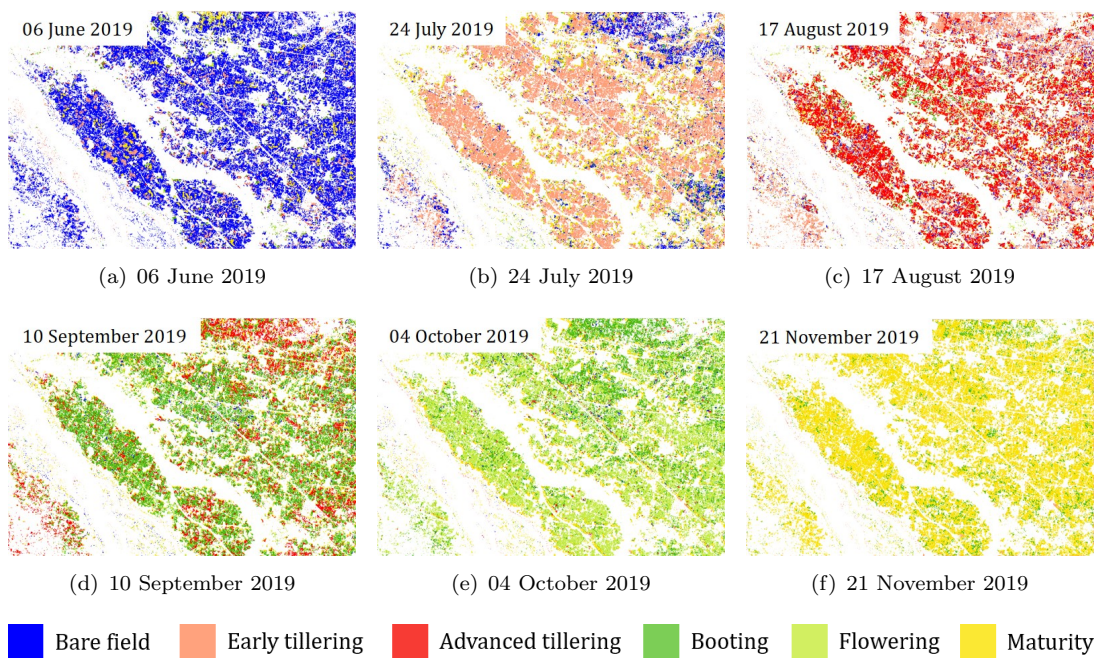


Figure 11. Variation of cluster using MF3CD scattering power components for the rice growing season with in the extent marked in yellow colour in Figure 1

Table 1. Radarsat-2 data acquired for the Indian test site

Acquisition date	Beam mode	Incidence angle range ($^{\circ}$)	Orbit	azimuth (m) \times range (m)
06 June 2019	FQ15W	33.73–36.65	Ascending	4.73×5.11
24 July 2019		33.73–36.65		
17 August 2019		33.73–36.65		
10 September 2019		33.73–36.65		
04 October 2019		33.73–36.64		
21 November 2019		33.73–36.64		

Table 2. Description of rice morphology at different growth stages

Date	Growth stage	Description
06 June 2019	Bare field (BF)	Complete soil layer is exposed with no standing crop
24 July 2019	Early tillering (ET)	1 to 3 tillers detectable
17 August 2019	Advanced tillering (AT)	Maximum number of tillers detectable
10 September 2019	Booting (B)	Flag leaf sheath swollen
04 October 2019	Flowering (F)	Anthers visible on most spikelets
21 November 2019	Maturity (M)	Grain becomes hard and plants appear yellowish

Table 3. Statistics (mean \pm standard deviation) of bio-physical and soil parameters at different phenology stages of rice. Here, PH: plant height, PAI: plant area index, SM: soil moisture and NA: No measurements available

Date	PH (cm)	PAI (m² m⁻²)	SM (%)	Growth stage
06 June 2019	NA	NA	31.92 ± 6.10	Bare field
24 July 2019	22.30 ± 3.21	0.60 ± 0.10	Saturated	Early tillering
17 August 2019	49.26 ± 7.12	1.86 ± 0.36	Saturated	Advanced tillering
10 September 2019	96.16 ± 8.76	6.03 ± 0.80	Saturated	Booting
04 October 2019	98.93 ± 4.76	6.16 ± 0.13	44.60 ± 0.72	Flowering
21 November 2019	99.32 ± 1.82	5.86 ± 0.62	41.16 ± 8.04	Maturity

Table 4. Producer’s and User’s accuracy of phenology stages of rice for MF3CF, An3D, F3D and Y3D decomposed power components using a RF classifier. BF: Bare field, ET: Early tillering, AT: Advanced tillering, B: Booting, F: Flowering, M: Maturity, PA: Producer’s accuracy, UA: User’s accuracy

	Methodology	Phenology stage					
		BF	ET	AT	B	F	M
PA	F3D(%)	85.41	78.04	69.44	69.23	81.81	73.33
	An3D(%)	79.17	80.48	91.67	82.06	90.90	70.00
	Y3D(%)	89.61	80.48	80.61	76.92	88.63	86.67
	MF3CF(%)	100.00	82.92	86.11	82.06	95.46	100.00
UA	F3D(%)	87.23	80.00	73.43	71.04	87.80	57.89
	An3D(%)	84.44	86.84	80.49	82.06	93.02	65.63
	Y3D(%)	84.31	84.61	82.86	76.92	90.69	83.87
	MF3CF(%)	94.11	94.44	77.60	86.48	95.47	100.00

Table 5. Global Measures for FP decomposition techniques

Method	Overall accuracy(%)	κ	p -value
F3D	76.89	0.73	1.76×10^{-7}
An3D	82.77	0.82	2.92×10^{-7}
Y3D	84.03	0.81	2.83×10^{-8}
MF3CF	91.17	0.91	1.84×10^{-8}

Table 6. Producer’s and User’s accuracy of phenology stages of rice for MF3CD, U2D and T_2 matrix elements using a RF classifier. BF: Bare field, ET: Early tillering, AT: Advanced tillering, B: Booting, F: Flowering, M: Maturity, PA: Producer’s accuracy, UA: User’s accuracy. The results are separately compared with MF3CF.

Methodology		Phenology stage					
		BF	ET	AT	B	F	M
PA	T_2 Elements(%)	82.92	79.48	59.61	57.60	82.06	64.86
	U2D(%)	87.80	84.62	64.28	65.00	82.04	75.67
	MF3CD(%)	95.83	80.48	83.33	89.47	90.90	100.00
	MF3CF(%)	100.00	82.92	86.11	82.06	95.46	100.00
UA	T_2 Elements(%)	97.14	75.61	80.64	52.27	91.43	46.16
	U2D(%)	97.29	80.49	81.82	63.41	91.43	54.90
	MF3CD(%)	95.83	91.67	83.33	87.18	93.02	70.60
	MF3CF(%)	94.11	94.44	77.60	86.48	95.47	100.00

Table 7. Global Measures for DP decomposition techniques

Method	Overall accuracy(%)	κ	p -value
T₂ Elements	71.00	0.66	3.93×10^{-8}
U2D	76.47	0.79	2.76×10^{-8}
MF3CD	86.97	0.84	1.93×10^{-8}
MF3CF	91.17	0.91	1.84×10^{-8}